Graphene Confers Ultralow Friction on Nanogear Cogs

Andrea Mescola, Guido Paolicelli, Sean P. Ogilvie, Roberto Guarino, James G. McHugh, Alberto Rota, Erica Iacob, Enrico Gnecco, Sergio Valeri, Nicola M. Pugno, Venkataramana Gadhamshetty, Maksud M. Rahman, Pulickel Ajayan,* Alan B. Dalton,* and Manoj Tripathi*

Friction-induced energy dissipation impedes the performance of nanomechanical devices. Nevertheless, the application of graphene is known to modulate frictional dissipation by inducing local strain. This work reports on the nanomechanics of graphene conformed on different textured silicon surfaces that mimic the cogs of a nanoscale gear. The variation in the pitch lengths regulates the strain induced in capped graphene revealed by scanning probe techniques, Raman spectroscopy, and molecular dynamics simulation. The atomistic visualization elucidates asymmetric straining of C—C bonds over the corrugated architecture resulting in distinct friction dissipation with respect to the groove axis. Experimental results are reported for strain-dependent solid lubrication which can be regulated by the corrugation and leads to ultralow frictional forces. The results are applicable for graphene covered corrugated structures with movable components such as nanoelectromechanical systems, nanoscale gears, and robotics.

1. Introduction

Engineering nanostructure through laser texturing, ion milling and photolithography has significantly improved the sensing performance of nano and microelectromechanical systems (NEMS and MEMS)[1,2] by tuning wetting characteristics,[3] nanochanneling,[4] optical,[5] mechanical,[6] and electronic properties.[7] The requirement for nano/micromachines has surged recently, with focus progressing toward miniaturized devices.[7,8] In the field of tribology, textured surfaces with micro or nanoscale dimples, grooves, pillars, and other geometries are found to be beneficial for optimized adhesion and friction forces.[9] Unlike macroscale textured surfaces,[10,11] the nanoscaled

A. Mescola, G. Paolicelli, A. Rota, S. Valeri
CNR-Istituto Nanoscienze - Centro S3
Via Campi 213, Modena 41125, Italy

S. P. Ogilvie, A. B. Dalton, M. Tripathi
Department of Physics and Astronomy
University of Sussex
Brighton BN1 9RH, UK
E-mail: a.b.dalton@sussex.ac.uk;
m.tripathi@sussex.ac.uk

R. Guarino
École Polytechnique Fédérale de Lausanne (EPFL)
Swiss Plasma Center (SPC)
Villigen PSI CH-5232, Switzerland

J. G. McHugh
Department of Chemistry
Loughborough University
Loughborough LE11 3TU, UK

A. Rota, S. Valeri
Department of Physics
Informatics and Mathematics
University of Modena and Reggio Emilia
Via Campi 213, Modena 41125, Italy

E. Iacob
Fondazione Bruno Kessler
Sensors and Devices
via Sommarive 18, Trento 38123, Italy

E. Gnecco
Marian Smoluchowski Institute of Physics
Jagiellonian University
Lojasiewicza 11, Krakow 30-348, Poland

N. M. Pugno
Laboratory of Bio-Inspired
Bionic, Nano, Meta, Materials and Mechanics
Department of Civil
Environmental and Mechanical Engineering
University of Trento
Via Mesiano, 77, Trento 38123, Italy

N. M. Pugno
School of Engineering and Materials Science
Queen Mary University of London
Mile End Road, London E1 4NS, UK

V. Gadhamshetty
Department Civil and Environmental Engineering
South Dakota School of Mines and Technology
Rapid City, SD 57701, USA

M. M. Rahman, P. Ajayan
Department of Materials Science and Nanoengineering
Rice University
Houston, TX 7705, USA
E-mail: pma2@rice.edu

structured geometry poses tremendous challenges for performance and efficiency when they are in physical contact with one another (e.g., gear operation at the nanoscale).[8] Interaction forces that are relatively weak at the macroscale (such as van der Waals and capillary forces) become dominant at the nanoscale. Therefore, nanostructured devices are often susceptible to conditions of extreme pressure, friction, and adhesion.[12] The nanoscale contacts exert enormous pressure at the interface even at low values of the applied normal force, subsequently leading to friction-induced wear.[13] Thus, a novel strategy is needed to regulate these forces at the nanoscale.

Several approaches have been adapted to tune the friction force by introducing liquid-state lubricants such as organic oils,[10,14] ionic liquids,[15,16] and tribological buffer layers such as polymer brushes.[17] Nevertheless, the ecologically harmful effect of liquid-state lubricants[18] and their inefficiency in confined conditions related to viscosity modifications hinder their tribological performance.[14] A potential alternative is presented by using solid-state lubricants,[19] in the form of nanoparticles or lamellar solids such as graphite, transition metal dichalcogenide (TMD), e.g., molybdenum disulfide[20,21] and recently reported the emerging class of MXenes (2D transition metal carbides, nitrides, and carbonitrides).[22] TMDs and MXenes have demonstrated impressive mechanical performance and potential for possible tribological applications.[23–25] One of the most promising solutions to protect surfaces at the nanoscale level relies on epitaxially grown graphene and its residue-free transfer technique.[26] Graphene has the lowest bending rigidity[27,28] coupled to high in-plane intrinsic strength[29] and is inert in humid and corrosive atmospheres.[30] However, the substrate on which graphene is deposited plays a pivotal role in modulating the mechanical, physical, and electronic properties.[31,32] In particular, strain induced by interaction with a substrate is one of the most intriguing parameters to adapt and tune graphene characteristics.[33,34] The role of substrate shape and its interfacial adhesion with graphene was theoretically studied by Wagner et al.,[35] who observed "snap-through" event of graphene under different textured confinements. They presented the transformation of graphene membrane from flat to conforming states relate to its bending rigidity which is useful to regulate the strain. The induced strain or strain gradient fields[36–38] correlate with tribological characteristics of graphene and other 2D materials (MoS_2) for strain-induced lubrication.[21] In another approach, modulation of frictional characteristics in graphene through functionalization (such as fluorination) is reported and hypothesized the role of flexural stiffness attributed to the higher frequency of flexural phonons for enhancing frictional signals.[39,40] Nevertheless, the results were limited in the consideration of generic elastic systems and adhesion force at the tip apex only. In the absence of functionalization, the increase in bending stiffness in 2D materials with adding atomic layer causes a decreases in friction dissipation, as thicker graphene is lesser susceptible to deform out-of-plane and ceased to adhere with tip.[41] Similarly, our previous work[42] demonstrated lowering of friction force for strongly covalently bonded interface for Gr/Ni (111) than weak van der Waals Gr/Silica interface due to lesser availability of graphene toward tip apex. Recently, the contact quality between suspended graphene and tip apex was also found to be altered through symmetrical

in-plane straining by depositing over circular-shaped textured structure in pressurized conditions to achieve a super lubricating state.[43] In spite of these significant results, the frictional response of asymmetrically-strained graphene over the textured surface remains a rarely addressed topic, which may play a crucial role in the durability of NEMS devices.

In the present study, we investigate the interplay between texture-induced strained graphene and its ability to lubricate. To do this, we employ nanotextured silicon surfaces as substrates that mimic the cogs of a nanogear and use friction force microscopy (FFM) measurements in ambient conditions to elucidate the effect of graphene deposition on the local friction properties. The different aspect ratios (depth/pitch) of the grooves modulate the conformation/suspension of graphene, resulting in it being strained. Raman spectroscopy shows the substrate-induced compressive strain in graphene over a flat surface, which systematically released as pitch length decreases. Molecular dynamics (MD) simulations corroborate the Raman measurements and elucidate the atomic-scale resolution of graphene corrugation. Simulation results identify an asymmetric strain distribution through lattice expansion and contraction of the C—C bond at different orientations. This work demonstrates, for the first time, the regulation of the frictional dissipation in nanoscale architecture through strain engineering of graphene.

2. Results and Discussion

Atomic force microscopy (AFM) images in **Figure 1**a–c show the typical morphology of graphene-covered textured surfaces referred to as GrP40, GrP125, and GrP250. The preparation and characterization of the textured surface is described in previous work[44,45] and in Section S1 Supporting Information. Each textured region comprises long parallel grooves ≈40 nm wide; the grooves' spacing referred to pitch length (P) varies from 40 ± 4, 125 ± 8, and 250 ± 14 nm. A chemical vapor deposition-grown single layer of graphene has been deposited over the textured surfaces by the wet transfer method.[46] The topographic profiles of bare and covered surfaces, presented in Figure 1d–f, illustrate the physical corrugation of graphene on the substrate. The measured depth of the grooves is between 2.4 and 3 nm on bare P40 is reduced by 10–15% after graphene deposition is measured from the bottom of trough. On the other hand, groove depths of bare P125 and P250 are ≈4 nm and are reduced by 7–10% in GrP125 and 3–5% GrP250, respectively, revealing higher conformation depth of graphene at GrP250. For GrP40 corrugation, suspension of graphene does not reach the stage of complete "snap-through;" and a partial conformal contact is achieved.[35] Thus, graphene can be considered as a membrane clamped between two grooves that induce different strains (see Figure S1, Supporting Information).

The conformation of graphene over the patterned surface unravels the mechanics as an act of balancing between interfacial adhesion and elastic energy stored in the graphene sheet (i.e., bending and stretching).[47,48] The conformation induced average transverse strain (ε) and interfacial adhesion energy (meV Å^{-2}) between graphene and textured surfaces, calculated from the height profiles, are reported in Figure 1g–i
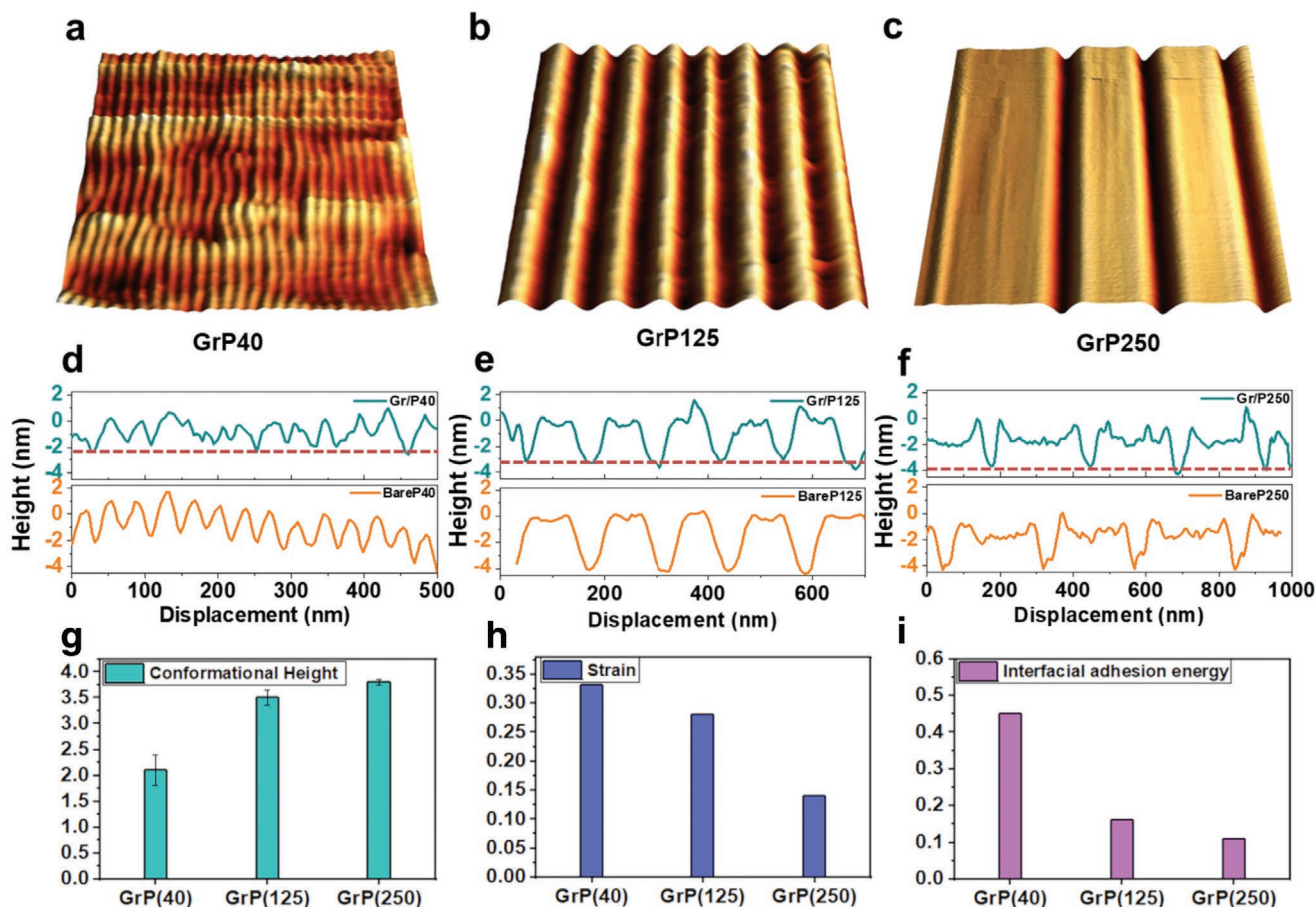
Figure 1. Morphology of graphene covered textured surfaces. AFM topography of graphene covered textured surface of pitch a) 40 ± 4 nm, b) 125 ± 5 nm, and c) 250 ± 8 nm. d–f) Topographical line profiles of bare and graphene covered textured surfaces across the grooves for covered (dark cyan) and bare surface (orange). The interfacial interaction between graphene and textured surfaces of different pitch lengths through g) conformational height, h) strain (%), and i) interfacial adhesion energy.

(see Section S2, Supporting Information for details). The systematic variations in the strain values indicating the contribution from the textured surfaces for their tendency to reduce compressive strain which is induced at the flat surface. The observation that the interaction (interfacial adhesion energy) between graphene and P40 is higher derives directly from the need of compensating a larger stretching energy (due to a corresponding larger compressive strain).[49]

The substrate-induced stretching/compression of single-layer graphene and the doping for each textured surface have been quantified by comparing Raman spectroscopy on the flat region (Gr/Flat) and graphene-covered textured surfaces (GrP40 to GrP250). The Raman modes of G peak position (PosG) and 2D peak position (Pos2D) are associated with strain, since a change in lattice constant leads to a variation in the phonon modes. Furthermore, these modes are useful for detecting carrier concentration (n) due to alteration in bond length and nonadiabatic electron–phonon coupling.[50] The relation between strain and doping of graphene with PosG and Pos2D is described in Section S3 in the Supporting Information. It is well recognized that physically deposited graphene on a flat Si substrate results in a p-type doped system under compressive strain.[51] The textured regions reduce the compressive strain in

graphene with smaller P values. This phenomenon is observed through gradual phonon softening of G and 2D Raman modes of graphene deposited over Gr/Flat, GrP250, and GrP40; see **Figure 2**a,b. Nevertheless, we did not observe the splitting of either G and 2D modes, which indicates that the magnitude of the induced strain is not appreciably high (<0.35%).[52]

The correlation plot in Figure 2c shows the distribution of Pos2D as a function of PosG with the mean value of the distribution represented by stars. The strain axis and doping axis are drawn at the slope (∂Pos2D/∂PosG) range 2.25–2.8 and 0.75, respectively.[53,54] The intersection of both axes is assumed to be a point of minimal strain and doping in suspended graphene with the coordinates taken from the work of Lee et al.[54] Thus, the distribution of all Raman data deviated from the intersection coordinates is used to predict strain and doping values. The correlation plot illustrates a relative change in the average compressive strain (ε) for Gr/flat of ≈−0.09%, which is transformed on corrugated surfaces as follows: $P = 250$ nm ($\varepsilon \approx −0.07\%$), $P = 125$ nm ($\varepsilon = −0.061\%$), $P = 40$ nm ($\varepsilon = 0.02\%$). This validates the argument of releasing compressive strain in graphene in the textured regions relative to the flat surface. It is worth noting that the Raman laser spot diameter using a 100X (objective lens) is ≈700 nm. Therefore, the measured strain
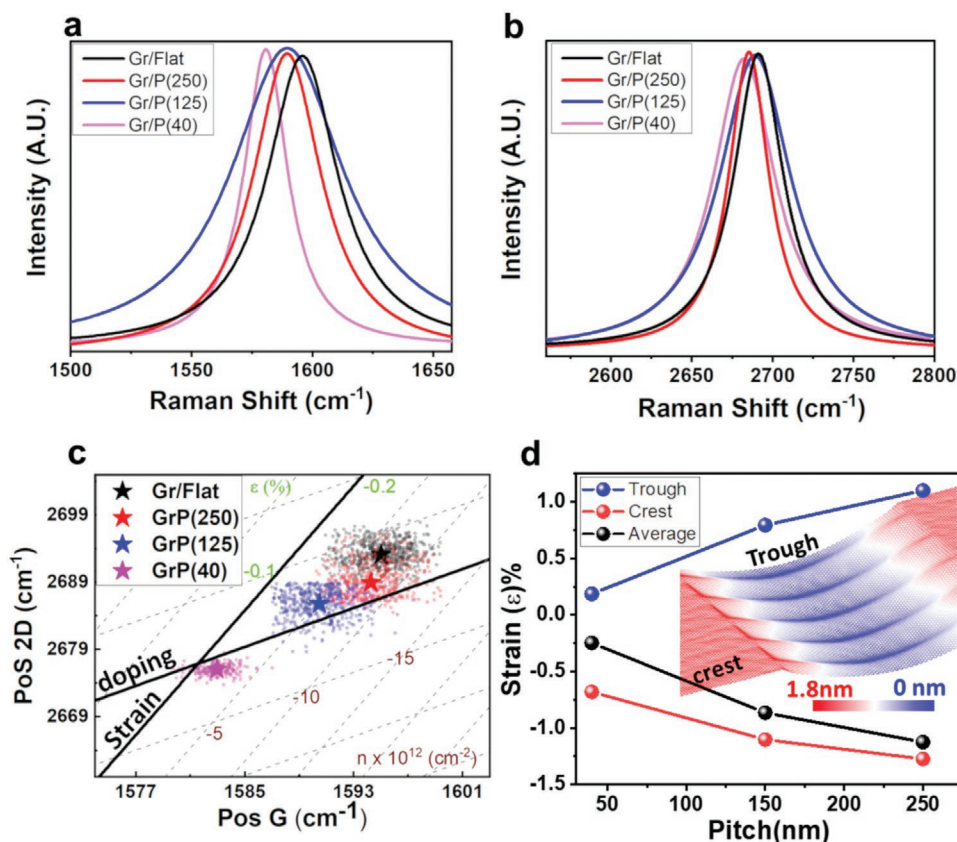
Figure 2. Raman spectrum of graphene covered textured region. Raman spectrum of a) PosG (cm^{-1}) and b) Pos2D (cm^{-1}) for graphene covered flat surface and different textured regions. c) Correlation plot of PosG versus Pos2D phonon modes for deconvoluted strain and doping in graphene from flat to the textured regions. The data distribution is from 50–70 Raman spectra and the mean values are represented by star-shaped points. The strain (ε) and doping (n) axis classify the distribution of Raman data. d) The bond strain distribution at the crest, trough and averaged over the entire surface (black color data) for different pitch lengths measured from MD simulations. Inset shows the net height (Z-scale) variation at crest and trough regions for GrP40 under the influence of net tensile and compressive strain.

and the carrier concentration values are averaged over several crests, troughs, and flat regions in each spectrum. Nevertheless, the distinct clusters of points in the correlation plots indicate the well-defined modulation of Raman modes and its associated strain and doping dictated by the substrate corrugation, Figure S2 in the Supporting Information. One can get a higher spatial resolution up to 25–40 nm and enhanced Raman scattering signals through tip-enhanced Raman spectroscopy for monitoring the contribution from the individual groove of the graphene covered textured surface.[55] This technique would be useful to investigate the change in the graphene lattice over the grooves and its associated electronic structure to be considered in near future.

Unlike flat or multiaxial-strained surfaces (e.g., suspended graphene over a circular trench), corrugated surfaces can induce anisotropy in strained graphene owing to the asymmetric stretching of carbon atoms oriented along parallel and perpendicular directions relative to the groove axis as found by Lee et al..[56] The atomic-scale features of the graphene conformation over the textured silicon surfaces have been investigated using MD and density functional theory (DFT) calculations of the Gr/Si at different pitch lengths, see Section S4 in the Supporting Information for DFT and MD setup. The crest region

of GrP250 shows higher compressive strain induced through contact with the Si substrate, while the neighboring trough exhibits curvature-induced tensile strain, which decreases with pitch length down to GrP40. The magnitude of the net compression over a crest is proportional to the area of the graphene in direct contact with the Si substrate and is therefore higher than the tension across the trough. This leads to a decreasing average value of compression, as shown in Figure 2d, which is in excellent agreement with our Raman spectroscopic measurements. A similar trend was observed by Zhang et al.[49] on biaxially-strained graphene covered self-assembled texturized silicon nanospheres with different diameters. In that arrangement, the authors reported a transformation of compressive strain into tensile strain in graphene deposited over smaller spherical particles due to the increasing real contact area at the apex. Hinnefeld et al.[53] found a similar trend for graphene suspended on silicon pillars with a separation distance of 600 nm indicating an increase in charge carrier concentration and decreased compressive strain. Here, by reducing the textured spacing by one order of magnitude (i.e., ≈ 40 nm), we find that the deposited graphene portrays characteristics of both strain and doping of a partially suspended sheet. The net height variation is illustrated in the inset Figure 2d (see scale bar). Notably, there is a
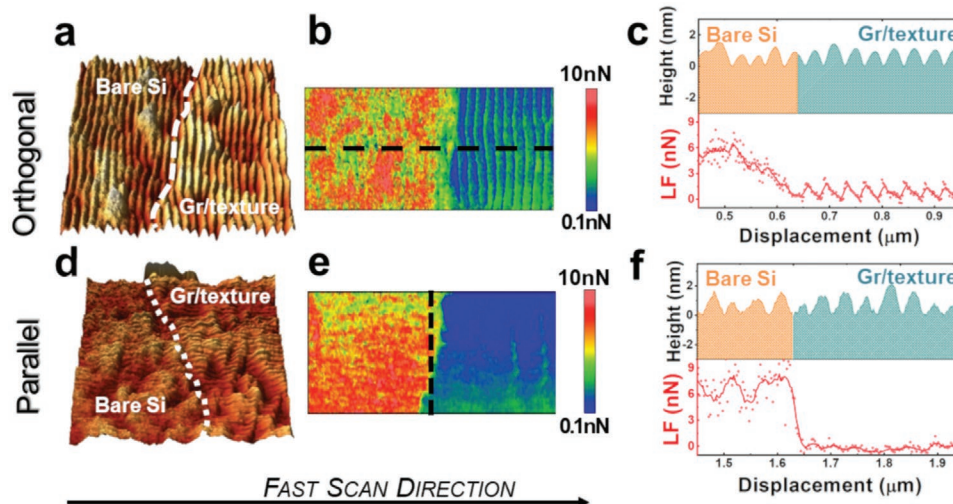
Figure 3. Effect of scan direction on friction force for GrP(40). First row shows a) topography image (1.0 × 1.0 μm²) and b) lateral force map (1.0 × 0.3 μm²) measured at applied normal load ≈30 nN on GrP40 for grooves axis aligned orthogonal to the fast scan direction. The white dashed line in topography profiles represents the interface between the bare and graphene covered region. c) Top: Height profile (orange color corresponds to bare silicon, dark cyan color to graphene covered region) and bottom: corresponding lateral force profile extracted from black dashed line in (b). Second-row shows d) topography image (1.0 × 1.0 μm²) and e) lateral force map (1.0 × 0.3 μm²) measured on GrP40 for groove axis aligned parallel to the fast scan direction at applied normal load ≈ 25 nN. f) Top: Height profile and bottom: corresponding lateral force profile extracted from black dashed line in (e).

generation of ripples in the suspended region due to the release of the net compressive strain. This phenomenon was further analyzed by FFM.

As Raman analysis suggests that the Gr/Flat and GrP(40) configurations provide the most pronounced differences in strain values, these extreme surfaces were chosen for FFM[57] measurements. Due to the intrinsic anisotropy in the texture-induced strain in graphene, FFM measurements were performed in orthogonal (**Figure 3**a–c) and parallel (Figure 3d–f) directions relative to the groove axis of GrP(40) (details about procedure and calibration are reported in Section S5, Supporting Information). The FFM images on the GrP40 sample comprise bare textured silicon regions and nearby graphene covered areas in a single acquisition. In this way, bare and covered textured surfaces are compared under similar contact conditions so that the local environment and possible geometrical effects or tip shape contributions can be disentangled (see Figure S5 in the Supporting Information for estimation of tip curvature radius). There is a significant contrast in the lateral force values between bare and covered graphene for both orientations (Figure 3b,e), which evidences the excellent lubrication performance of single-layer graphene over the periodic surface. The presence of graphene reduces the average friction force up to ten times compared to the bare surface under similar applied load conditions ranging from 10–30 nN, with no edge failure noticeable. These results are in agreement with previous nanotribological characterizations of graphene on flat silicon substrates.[58–60] Friction force values are also lower than on crystal and polycrystalline chemical vapor deposition (CVD) MoS_2[25] and comparable to hBN/silica.[61] The lateral force profile in Figure 3c shows a markedly distinguishable undulated friction force response between graphene-covered and bare silicon, orthogonal to the groove axis. Here, the lateral force is significant with stochastic variation over the bare silicon but is

reduced and periodically modulated in the graphene capped region.

While scanning parallel to the groove axis at the capped region, friction force modulation as a function of tip displacement is almost zero, though stochastic lateral force is sustained at the bare surface. This is clearly illustrated in the lateral force map in Figure 3e and in the profile drawn orthogonal to the groove axis (Figure 3f) to provide a valid comparison with Figure 3c. The detailed analysis between crest and trough for the scanned orthogonal and parallel reveals a remarkable difference (Gr/$LF_{Trough\ parallel}$ − Gr/$LF_{crest\ parallel}$) ≈ 0.2 nN and (Gr/$LF_{Trough\ orthogonal}$ − Gr/$LF_{crest\ orthogonal}$) ≈ 1.5 nN; a more than sevenfold increase. The ratio of the friction force at trough/crest measured during the scan in parallel and orthogonal directions at fixed load conditions is ≈2 and 5, respectively. Thus, the trough region of an orthogonally-scanned textured surface contributes to the highest lateral force, but this effect is suppressed along the parallel-scanned region. On the other hand, the frictional response over the bare Si textured surface scanned in orthogonal and parallel directions is isotropic, as expected for this design of texturing.[62] This indicates that the anisotropic strain distribution in the graphene monolayer plays a pivotal role in regulating the friction force induced from the textured surface.

The texture-induced straining in graphene, undulating friction dissipation and anisotropic sliding resistance over the groove axis could be useful in regulating the motion of nanoscale objects, in engineering designer diffusion gradients for adsorbed molecules or even as a smart substrate to effect the proliferation of biological cells for tissue engineering applications. Such a high degree of friction force regulation is not possible over flat surfaces coated in graphene, which shows similar friction force (isotropic) in different scanning directions, (see Figure S6, Supporting Information). While,
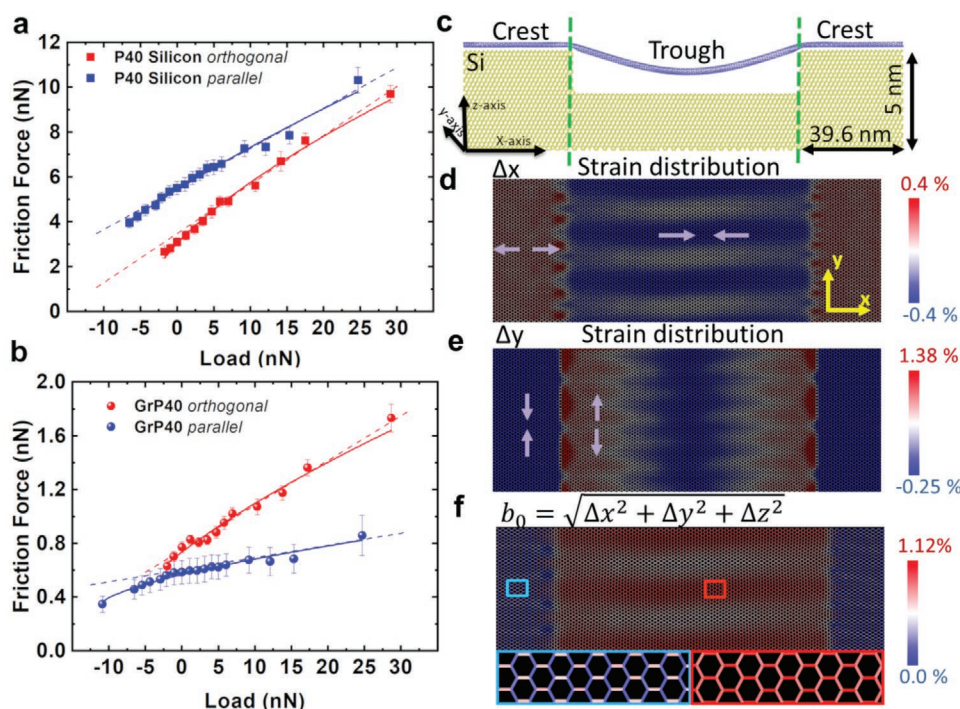
Figure 4. Friction force as a function of load applied to groove axis and strain distribution: Experimental data of load dependent friction force curves on GrP40 sample with the grooves axis oriented parallel (blue) and perpendicular (red) to the fast scan direction: a) on bare silicon textured surface and b) on adjacent graphene covered region. Square and circular shaped data represent the experimental values, continuous lines are the fitting curve from DMT model and dashed line is the linear fit. c) MD simulation of a graphene sheet sags into the P40 textured Si surface. The vertical drawn dashed green lines represent the trough region of suspended graphene between two crests. d) Strain distribution based on bond strain variation along the x-axis (Δx), e) y-axis (Δy), and f) total bond length (b_0). The inset region (marked by the colored rectangle in panel (f)) shows the variation in C–C bond length in the crest and trough regions. The asymmetry in b_0 between different regions and along different axes is readily apparent, as shown in the zoom-in image.

frictional anisotropy is also reported through different arrangements of carbon atoms in graphene,[63,64] here we demonstrate friction force regulation through the graphene-covered textured substrate as a versatile post-treatment for surfaces in nanomechanical devices.

The load dependence friction curves for P(40) and GrP(40) are reported in **Figure 4** for orthogonal- and parallel-scanned directions (see details in Section S6 and Figure S7–S9, Supporting Information). The friction force values for the bare textured region are increased by a factor of 10 as compared to graphene-covered regions for all applied loads range (−10 to 30 nN), consistent with the lateral force profile. The shear strength (S = friction force/area) of the interface is measured by fitting the data through the Derjaguin–Muller–Toporov (DMT) model (continuous line in Figure 4a,b) following 2/3 power law within continuum mechanical modeling of the contact region[65–67] and the coefficient of friction (COF) is measured by a linear fit of the curves (dashed lines). The use of DMT approximation is justified due to low adhesion force at the interfacial contact. Nevertheless, these contact conditions could alter depending on the magnitude of local adhesion force, where different contact conditions, e.g., Johnson–Kendall–Roberts can be implemented as reported by Deng et al.[59] and Lang et al.[68] The results are shown in **Figure 5**, revealing a factor of three change in the S(MPa) for GrP40 between parallel and orthogonal directions to the groove axis (38/12 ≈ 3.16). In contrast, S measured for

bare P40 for scanned parallel and orthogonal directions found comparable (345/322 ≈ 1.07). Also, S measured for sliding parallel to the groove on GrP40 ($S ≈ 12$ MPa) is lower by ≈50% than Gr/Flat (for $S ≈ 25$ MPa), which is in good agreement with the literature.[59,69]

The COF values are corroborated with S revealing minimal values of 0.009 ± 0.001 and 0.011 ± 0.002 at different locations respectively. The COF values for the Gr/Flat surface were found to be intermediate between the orthogonal and parallel scanned axis. Our results are in good agreement with the investigation presented by Zhang et al.[43] on tuning the COF by regulating strain in the suspended graphene. The reported COF of the suspended graphene (a region of low strain) is almost double compared to
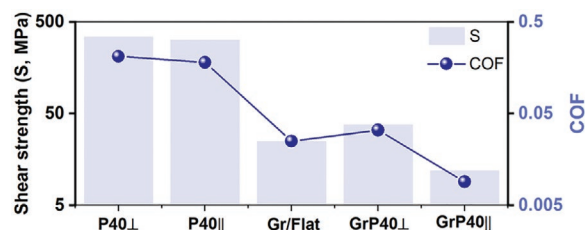

Figure 5. Shear strength (MPa) and COF values of nanogear. The modulation in the shear strength (S, MPa) and COF values at different scanning directions. Graphene on a flat surface lies intermediate values between scanning parallel (∥) and perpendicular (⊥) to the groove axis.

that of strained (0.3%) graphene. The presented textured surfaces demonstrate that crests and troughs serve as distinct strained regions that can regulate the friction force. The FFM values for Gr/Flat represent a compressive strain system, as demonstrated in the Raman correlation plot. Here, sliding of tip under finite normal force leads to elastic buckle formation as a "puckering" effect which leads to the higher friction force values.[41]

The anisotropic values of the friction force for the graphene covered textured surface can be explained through anisotropic stretching/compression of C−C bonds in orthogonal directions over an individual groove. It has been validated through MD simulation for graphene over P40 architecture, as shown in Figure 4c. The carbon-silicon interaction has been implemented using a Lennard Jones 6–12 potential with ε (Si-C) = 8.909 meV and σ (Si-C) = 0.3326 nm to model physisorption of the graphene monolayer on a silicon substrate.[70,71] The strain distribution in graphene over the crest and trough (between green dashed lines in panel (c)) in orthogonal (x), parallel (y), and out-of-plane to the silicon surface has been calculated through percentage changes in Δx, Δy and bond length $b_o = \sqrt{\Delta x^2 + \Delta y^2 + \Delta z^2}$ with respect to Gr/Flat (see Section S4, Supporting Information for details), respectively, and is shown in Figure 4d–f. Along the x-axis, the carbon atoms of graphene at a crest are continually stretched until the crest–trough interface is reached (red color). The localized stretching of C−C bonds at the interface leads to a net compressive strain distribution at the trough of equal magnitude, see scale bar at Figure 4d. Along the y-axis, the crest region weakly compresses the C−C bond in contrast to the Δx strain distribution, but a significant tensile strain dominates from interface to the trough region. Thus, there is a net tensile strain resulting from the combined effect of substrate adhesion and adjacent suspended graphene (see Figure 4e).

The integral bond length (b_o) distribution at the crest illustrates asymmetric bond alteration along the orthogonal (stretching) and parallel (compressive) directions relative to the groove axis. This asymmetry is also sustained at the trough, but a higher magnitude observed (see Figure 4f) and its inset marked by rectangles. Thus, the friction force is lowest whilst sliding perpendicular to the stretched axis of graphene. Also, this distinction in the bond length distribution results in anisotropy in friction forces orthogonal and parallel to the groove axis. It clearly shows the remarkable anisotropic tribological (friction force, COF, S) performance of graphene over the same textured surface, which is not possible for a traditional Gr/Flat system. Thus, graphene covered textured systems could bring an era of tuned friction force in nanoscale, which has been a nontrivial task in the last decades. Moreover, such regulated friction could enhance the performance of nanomachines.

3. Conclusion

In summary, the deposition of graphene over textured silicon surfaces can offer a wide range of opportunities due to the interplay between adhesion force energy, bending, stretching, and strained orientation. By controlling the groove separation distance in the substrate, a tunable strain in a single layer of graphene can be achieved, presented through the analytical

modeling, MD simulation, and Raman spectroscopic measurements. The graphene deposited over a flat Si surface undergoes compressive strain, which is released over the textured surfaces. The overlayered graphene also drops the friction force values at the extent of extreme lubricity and channelizes the friction dissipation while sliding, complementary to the textured geometry. The strain distribution in graphene over the textured architecture regulates the friction force; consequently, COF and S values. Thus, single-layer graphene deposited onto an anisotropic nanotextured system could acquire diverse nanomechanical properties. It is demonstrated in reference to the FFM that depends on the sliding direction with respect to grooves orientation. The presented work will pave the pathway to nanoscale devices for efficient functioning and controlled motion of nanoscale objects, particularly in nanomechanical devices and nanorobotics.

4. Experimental Section

Deposition of Graphene over Textured Surface: Commercially available single-layer CVD graphene from Advanced Chemicals Supplier Material (Pasadena, CA, USA) and Graphenea Inc. (Spain) were deposited on nanostructured surfaces through the standard method of polymethylmethacrylate polymer assisted wet transfer followed by removal of polymer residue in an acetone bath (40 °C for 30 min). Later, samples were dried in the oven at 40 °C for 20 min and sequentially heated in a vacuum at 300 °C for 2 h. The validation of distribution of single graphene layer is carried out by Raman spectroscopy, where peak intensity of Raman modes measured 2D/G >1.3. AFM assisted mechanical cleaning have been conducted by a sacrificial cantilever prior to the friction measurements.

Raman Measurements: Raman spectroscopy is carried out by using a Renishaw inVia confocal Raman microscope. The laser line used for the investigation was λ = 532 nm (Source: Solid-state, model RL53250) and 1800 groove mm^{-1} grating. All the measurements were performed at 10% laser power (controlled through neutral density filters) with 5 s exposure at 100X magnification. This setup can provide the spectral resolution up to 0.3 cm^{-1} and the penetration depth up to 0.7–0.93 μm for Si wafer,[72] which is sufficient for the investigation. The Raman modes of G and 2D peaks are fitted with Lorentzian curve to evaluate the peak positions (cm^{-1}) and peak intensity.

Atomic Force Microscopy and Friction Force Microscopy: Two different atomic force microscopes (AFM) were utilized during the experiments. The Bruker Dimension Icon with Peak Force Tapping Mode option and the NT-MDT NTEGRA AURA system. All the measurements were carried out in air, under ambient conditions. Commercially available rectangular shaped silicon cantilevers (MikroMaschHQ: CSC37/NoAl) with nominal normal elastic constants between 0.2 and 0.8 N m^{-1} were used for FFM measurements. The detailed calibration procedure for the measurements is mentioned in Section S5 in the Supporting Information.

Supporting Information

Supporting Information is available from the Wiley Online Library or from the author.

Acknowledgements

Conflict of Interest

The authors declare no conflict of interest.

Data Availability Statement

Research data are not shared.

Keywords

[1] A. Balčytis, J. Juodkazytė, G. Seniutinas, X. Li, G. Niaura, S. Juodkazis, in *Laser-based Micro- and Nanoprocessing X*, Vol. *9736* (Eds: U. Klotzbach, K. Washio, C. B. Arnold), **2016**, p. 97360G.

[2] X. Zang, Q. Zhou, J. Chang, Y. Liu, L. Lin, *Microelectron. Eng.* **2015**, *132*, 192.

[3] J. Bico, U. Thiele, D. Quéré, *Colloids Surf., A* **2002**, *206*, 41.

[4] C. Cottin-Bizonne, J.-L. Barrat, L. Bocquet, E. Charlaix, *Nat. Mater.* **2003**, *2*, 237.

[5] L. A. Dobrzański, A. Drygała, K. Gołombek, P. Panek, E. Bielańska, P. Zieba, *J. Mater. Process. Technol.* **2008**, *201*, 291.

[6] K. J. Hemker, W. N. Sharpe Jr, *Annu. Rev. Mater. Res.* **2007**, *37*, 93.

[7] S. Finkbeiner, in *2013 Proceedings of the ESSCIRC (ESSCIRC)*, IEEE, Piscataway, NJ **2013**, p. 9.

[8] S. Mukherjee, N. R. Aluru, *Applications in Micro- and Nano-electromechanical Systems*, Engineering Analysis with Boundary Elements, Vol. *30*, Elsevier, The Netherland **2006**, p. 909.

[9] Y.-Z. Hu, T.-B. Ma, in *Comprehensive Nanoscience and Technology*, Elsevier, New York **2011**, Vol. *1–5*, pp. 383–418.

[10] Y. Xue, X. Shi, Q. Huang, K. Zhang, C. Wu, *Tribol. Int.* **2021**, *161*, 107099.

[11] L. Rapoport, A. Moshkovich, V. Perfilyev, I. Lapsker, G. Halperin, Y. Itovich, I. Etsion, *Surf. Coat. Technol.* **2008**, *202*, 3332.

[12] Y. Ping, L. N. Bo, Y. Daoguo, L. J. Ernst, *Microsyst. Technol.* **2006**, *12*, 1125.

[13] M. Tripathi, F. Awaja, R. A. Bizao, S. Signetti, E. Iacob, G. Paolicelli, S. Valeri, A. Dalton, N. M. Pugno, *ACS Appl. Mater. Interfaces* **2018**, *10*, 44614.

[14] J. Klein, E. Kumacheva, *Science* **1995**, *269*, 816.

[15] O. Y. Fajardo, F. Bresme, A. A. Kornyshev, M. Urbakh, *Sci. Rep.* **2015**, *5*, 7698.

[16] A. A. Al-Azizi, O. Eryilmaz, A. Erdemir, S. H. Kim, *Langmuir* **2013**, *29*, 13419.

[17] S. Lee, N. D. Spencer, *Science* **2008**, *319*, 575.

[18] O. Hod, E. Meyer, Q. Zheng, M. Urbakh, *Nature* **2018**, *563*, 485.

[19] A. Rosenkranz, H. L. Costa, M. Z. Baykara, A. Martini, *Tribol. Int.* **2021**, *155*, 106792.

[20] K. C. Mutyala, Y. a. Wu, A. Erdemir, A. V. Sumant, *Carbon N. Y.* **2019**, *146*, 524.

[21] C. Wang, H. Li, Y. Zhang, Q. Sun, Y. Jia, *Tribol. Int.* **2014**, *77*, 211.

[22] B. C. Wyatt, A. Rosenkranz, B. Anasori, *Adv. Mater.* **2021**, *33*, 2007973.

[23] M. Malaki, R. S. Varma, *Adv. Mater.* **2020**, *32*, 2003154.

[24] A. Rodriguez, M. S. Jaman, O. Acikgoz, B. Wang, J. Yu, P. G. Grützmacher, A. Rosenkranz, M. Z. Baykara, *Appl. Surf. Sci.* **2021**, *535*, 147664.

[25] F. Lavini, A. Calò, Y. Gao, E. Albisetti, T.-D. Li, T. Cao, G. Li, L. Cao, C. Aruta, E. Riedo, *Nanoscale* **2018**, *10*, 8304.

[26] K. Yong, A. Ashraf, P. Kang, S. Nam, *Sci. Rep.* **2016**, *6*, 24890.

[27] D.-B. Zhang, E. Akatyeva, T. Dumitrică, *Phys. Rev. Lett.* **2011**, *106*, 255503.

[28] H. Chen, S. Chen, *J. Phys. D: Appl. Phys.* **2013**, *46*, 435305.

[29] M. R. Vazirisereshk, H. Ye, Z. Ye, A. Otero-de-la-Roza, M. - Q. Zhao, Z. Gao, A. T. C. Johnson, E. R. Johnson, R. W. Carpick, A. Martini, *Nano Lett.* **2019**, *19*, 5496.

[30] G. Chilkoor, N. Shrestha, A. Kutana, M. Tripathi, F. C. Robles Hernández, B. I. Yakobson, M. Meyyappan, A. B. Dalton, P. M. Ajayan, M. M. Rahman, V. Gadhamshetty, *ACS Nano* **2021**, *3987*, 447.

[31] K.-S. Kim, H.-J. Lee, C. Lee, S.-K. Lee, H. Jang, J.-H. Ahn, J.-H. Kim, H.-J. Lee, *ACS Nano* **2011**, *5*, 5107.

[32] M. Tripathi, F. Lee, A. Michail, D. Anestopoulos, J. G. McHugh, S. P. Ogilvie, M. J. Large, A. A. Graf, P. J. Lynch, J. Parthenios, K. Papagelis, S. Roy, M. A. S. R. Saadi, M. M. Rahman, N. M. Pugno, A. A. K. King, P. M. Ajayan, A. B. Dalton, *ACS Nano* **2021**, *15*, 2520.

[33] A. M. van der Zande, R. A. Barton, J. S. Alden, C. S. Ruiz-Vargas, W. S. Whitney, P. H. Q. Pham, J. Park, J. M. Parpia, H. G. Craighead, P. L. McEuen, *Nano Lett.* **2010**, *10*, 4869.

[34] N. Levy, S. A. Burke, K. L. Meaker, M. Panlasigui, A. Zettl, F. Guinea, A. H. C. Neto, M. F. Crommie, *Science* **2010**, *329*, 544.

[35] T. J. W. Wagner, D. Vella, *Appl. Phys. Lett.* **2012**, *100*, 233111.

[36] X. Wang, K. Tantiwanichapan, J. W. Christopher, R. Paiella, A. K. Swan, *Nano Lett.* **2015**, *15*, 5969.

[37] C. Wang, S. Chen, *Sci. Rep.* **2015**, *5*, 13675.

[38] C. Dai, Z. Guo, H. Zhang, T. Chang, *Nanoscale* **2016**, *8*, 14406.

[39] S. Kwon, J.-H. Ko, K.-J. Jeon, Y.-H. Kim, J. Y. Park, *Nano Lett.* **2012**, *12*, 6043.

[40] J.-H. Ko, S. Kwon, I.-S. Byun, J. S. Choi, B. H. Park, Y.-H. Kim, J. Y. Park, *Tribol. Lett.* **2013**, *50*, 137.

[41] C. Lee, Q. Li, W. Kalb, X. Z. Liu, H. Berger, R. W. Carpick, J. Hone, *Science* **2010**, *328*, 76.

[42] G. Paolicelli, M. Tripathi, V. Corradini, A. Candini, S. Valeri, *Nanotechnology* **2015**, *26*, 055703.

[43] S. Zhang, Y. Hou, S. Li, L. Liu, Z. Zhang, X.-Q. Feng, Q. Li, *Proc. Natl. Acad. Sci. U. S. A.* **2019**, *116*, 24452.

[44] A. Rota, M. Tripathi, G. Gazzadi, S. Valeri, *Langmuir* **2013**, *29*, 5286.

[45] R. Dell'Anna, E. Iacob, M. Tripathi, A. Dalton, R. Böttger, G. Pepponi, *J. Microsc.* **2020**, *280*, 183.

[46] A. Pirkle, J. Chan, A. Venugopal, D. Hinojos, C. W. Magnuson, S. McDonnell, L. Colombo, E. M. Vogel, R. S. Ruoff, R. M. Wallace, *Appl. Phys. Lett.* **2011**, *99*, 2009.

[47] J. S. Bunch, M. L. Dunn, *Solid State Commun.* **2012**, *152*, 1359.

[48] W. G. Cullen, M. Yamamoto, K. M. Burson, J.-H. Chen, C. Jang, L. Li, M. S. Fuhrer, E. D. Williams, *Phys. Rev. Lett.* **2010**, *105*, 215504.

[49] Y. Zhang, M. Heiranian, B. Janicek, Z. Budrikis, S. Zapperi, P. Y. Huang, H. T. Johnson, N. R. Aluru, J. W. Lyding, N. Mason, *Nano Lett.* **2018**, *18*, 2098.

[50] M. Lazzeri, F. Mauri, *Phys. Rev. Lett.* **2006**, *97*, 266407.

[51] S. Goniszewski, M. Adabi, O. Shaforost, S. M. Hanham, L. Hao, N. Klein, *Sci. Rep.* **2016**, *6*, 22858.

[52] C. Kong, C. Pilger, H. Hachmeister, X. Wei, T. H. Cheung, C. S. W. Lai, N. P. Lee, K. K. Tsia, K. K. Y. Wong, T. Huser, *Light: Sci. Appl.* **2020**, *9*, 1.

[53] J. H. Hinnefeld, S. T. Gill, N. Mason, *Appl. Phys. Lett.* **2018**, *112*, 173504.

[54] J. E. Lee, G. Ahn, J. Shim, Y. S. Lee, S. Ryu, *Nat. Commun.* **2012**, *3*, 1024.

[55] M. V. Balois, N. Hayazawa, S. Yasuda, K. Ikeda, B. Yang, E. Kazuma, Y. Yokota, Y. Kim, T. Tanaka, *npj 2D Mater. Appl.* **2019**, *3*, 38.

[56] J. K. Lee, S. Yamazaki, H. Yun, J. Park, G. P. Kennedy, G. T. Kim, O. Pietzsch, R. Wiesendanger, S. Lee, S. Hong, U. Dettlaff-Weglikowska, S. Roth, *Nano Lett.* **2013**, *13*, 3494.

[57] E. Gnecco, R. Pawlak, M. Kisiel, T. Glatzel, E. Meyer, in *Nanotribology and Nanomechanics*, Springer International Publishing, Cham **2017**, pp. 519–548.

[58] S. Zhang, T. Ma, A. Erdemir, Q. Li, *Mater. Today* **2019**, *26*, 67.

[59] Z. Deng, N. N. Klimov, S. D. Solares, T. Li, H. Xu, R. J. Cannara, *Langmuir* **2013**, *29*, 235.

[60] N. Manini, G. Mistura, G. Paolicelli, E. Tosatti, A. Vanossi, *Adv. Phys. X* **2017**, *2*, 569.

[61] P. Gallagher, M. Lee, F. Amet, P. Maksymovych, J. Wang, S. Wang, X. Lu, G. Zhang, K. Watanabe, T. Taniguchi, D. Goldhaber-Gordon, *Nat. Commun.* **2016**, *7*, 10745.

[62] A. Berardo, G. Costagliola, S. Ghio, M. Boscardin, F. Bosia, N. M. Pugno, *Mater. Des.* **2019**, *181*, 107930.

[63] C. M. Almeida, R. Prioli, B. Fragneaud, L. G. Cançado, R. Paupitz, D. S. Galvão, M. De Cicco, M. G. Menezes, C. A. Achete, R. B. Capaz, *Sci. Rep.* **2016**, *6*, 31569.

[64] J. S. Choi, J.-S. Kim, I.-S. Byun, D. H. Lee, M. J. Lee, B. H. Park, C. Lee, D. Yoon, H. Cheong, K. H. Lee, Y.-W. Son, J. Y. Park, M. Salmeron, *Science* **2011**, *333*, 607.

[65] R. W. Carpick, D. F. Ogletree, M. Salmeron, *Area* **1999**, *400*, 395.

[66] U. D. Schwarz, O. Zwörner, P. Köster, R. Wiesendanger, *Phys. Rev. B: Condens. Matter Mater. Phys.* **1997**, *56*, 6997.

[67] T. D. B. Jacobs, A. Martini, *Appl. Mech. Rev.* **2017**, *69*, 060802.

[68] H. Lang, Y. Peng, X. Cao, K. Zou, *ACS Appl. Mater. Interfaces* **2020**, *12*, 25503.

[69] R. Buzio, A. Gerbi, S. Uttiya, C. Bernini, A. E. Del Rio Castillo, F. Palazon, A. S. Siri, V. Pellegrini, L. Pellegrino, F. Bonaccorso, *Nanoscale* **2017**, *9*, 7612.

[70] M. Kaftory, M. Kapon, M. I. Botoshansky, *The Chemistry of Organic Silicon Compounds*, Vol. *121*, Wiley, Chichester **1998**, p. 181.

[71] J. H. Los, A. Fasolino, *Phys. Rev. B* **2003**, *68*, 024107.

[72] Z. Xu, Z. He, Y. Song, X. Fu, M. Rommel, X. Luo, A. Hartmaier, J. Zhang, F. Fang, *Micromachines* **2018**, *9*, 361.

Graphene Confers Ultralow Friction on Nanogear Cogs

Andrea Mescola, Guido Paolicelli, Sean P. Ogilvie, Roberto Guarino, James G. McHugh, Alberto Rota, Erica Iacob, Enrico Gnecco, Sergio Valeri, Nicola M. Pugno, Venkataramana Gadhamshetty, Maksud M. Rahman, Pulickel Ajayan,* Alan B. Dalton,* and Manoj Tripathi*

Supporting Information

Graphene confers ultra-low friction on nanogear cogs

Andrea Mescola[1#], Guido Paolicelli[1#], Sean P. Ogilvie[2$], Roberto Guarino[3$], James G. McHugh[4], Alberto Rota[1,5], Erica Iacob[6], Enrico Gnecco[7], Sergio Valeri[1,5], Nicola M. Pugno[8, 9], Venkataramana Gadhamshetty[10], Maksud M. Rahman[11], Pulickel Ajayan[11*], Alan B. Dalton[2*], Manoj Tripathi[2*]

[1] CNR-Istituto Nanoscienze - Centro S3, Via Campi 213 41125 Modena, Italy

[2] Department of Physics and Astronomy, University of Sussex, Brighton BN1 9RH, U.K.

[3] École Polytechnique Fédérale de Lausanne (EPFL), Swiss Plasma Center (SPC), CH-5232 Villigen PSI, Switzerland

[4] Department of Chemistry, Loughborough University, Loughborough LE11 3TU, United Kingdom

[5] Department of Physics, Informatics and Mathematics, University of Modena and Reggio Emilia, Via Campi 213 41125 Modena, Italy

[6] Fondazione Bruno Kessler, Sensors and Devices, via Sommarive 18, 38123 Trento, Italy

[7] Otto Schott Institute of Materials Research, Friedrich Schiller University Jena, D-07743 Jena, Germany

[8] Laboratory of Bio-Inspired, Bionic, Nano, Meta, Materials & Mechanics, Department of Civil, Environmental and Mechanical Engineering, University of Trento, Via Mesiano, 77, 38123 Trento, Italy

[9] School of Engineering and Materials Science, Queen Mary University of London, Mile End Road, London E1 4NS, UK

[10] Department Civil and Environmental Engineering, South Dakota School of Mines and Technology, Rapid City, South Dakota 57701, USA

[11] Department of Materials Science and Nanoengineering, Rice University, Houston, TX 7705, USA

1. **Morphology Characterization and conformation**
2. **Estimation of strain and adhesion energy**
3. **Calculation of strain and doping from Raman modes in Graphene**
4. **Molecular Dynamics and density functional theory**
5. **AFM and FFM calibration**

6. Friction vs load curves fitting procedure

S1. Morphology Characterization and conformation

<u>P(40) sample</u>

Preparation of textured surface: Texture of the P(40) sample was obtained by low energy ion irradiation of a (100) silicon wafer over 1×1 cm^2 area. Ion beam parameters (1 keV O+ ion beams, with fluxes 1.1×10^{13} cm^{-2} s^{-1} and angle of incidence of 50°) were optimized to obtain a texture of quasi parallel grooves with nanometer height. Texture of the P(125) and P(250) samples was obtained by focused ion beam (FIB) milling of a (001) silicon wafer (P doped, resistivity 500−3000 Ω cm). Milling was performed with a dual beam FIB apparatus (FEIDB235M) using a 30KeV Ga+ ion beam at normal incidence with ion dose of 2.25 x 10^{16} ions/cm^2. The resulting structure were square-textured areas (10µm $\times$ 10µm) composed of parallel nano-grooves about 50 nm wide with variable pitches of 125 and 250 nm. The optimization of FIB milling procedure have been reported in our previous work (ref. 44 in main text). We did not observe any significant differences in the COF values for irradiated and flat regions indicating the minimal effect of Ga ions deposition in the friction force.

Sample was characterized by AFM using semi-contact mode imaging in air. The period of the texture structure along the direction of incident ions was calculated as the first maximum of height-height Auto Correlation Function (ACF), and it result about 40 ± 2 nm. The height of the grooves h i.e. the average difference between peak heights and valley depths of the grooves, calculated as the maximum vertical distances between the highest and lowest data points within one period and for all the possible periods contained in a single row. The optimization of low energy ion irradiation procedure as well as the characterization methods have been comprehensively discussed elsewhere [1,2].

S2. Estimation of strain and adhesion energy

The AFM profile of the substrate and the deformed shape of the graphene sheet can be approximated by a sinusoidal function (for the 40 nm-pitch profile) and by the trapezoidal shape depicted below (for the 125 and 250 nm-pitch profiles). Considering only one period as an example, the graphene sheet can be assumed to have a length equal to the wavelength λ in the undeformed shape (i.e., it is completely flat before the interaction with the substrate). After deformation, the new length of the graphene sheet in the x-y plane is given, for the 40nm-pitch profile by eq (1a):

$$l' = \int_L y_G(x)\, dx = \int_0^\lambda \sqrt{1 + \left(\frac{\partial y_G}{\partial x}\right)^2}\, dx \tag{1a}$$

and, for the 125 and 250 nm-pitch profiles, by eq (1b):

$$l' = 2\delta_1 + 2\delta_2 \tag{1b}$$

where $y_G(x) = A \sin\left(\frac{2\pi}{\lambda} x\right)$, while the parameters δ_1 and δ_2 define the regions of the graphene sheets that adhere to the substrate (i.e., conformed). In this way, we take into account that only the 40 nm-pitch profile produces a suspended graphene sheet, as observed from the morphology data (**Figure 1** in the main text).

Consequently, the average strain due to in-plane stretching can be measured as:

$$\varepsilon_x = \frac{l' - \lambda}{\lambda} \tag{2}$$

It is based on the assumption that whole graphene sheet undergoes a tensile strain in the x direction (i.e. perpendicular to the groove axis). This could be seen as a relative strain, since it does not consider the "reference" compressive strain ε_c of a generic graphene sheet on a flat substrate.

In order to estimate the adhesion energy, an explicit expression of the average strain is needed for all the three considered substrates. Therefore, the trapezoidal profile introduced above must be used also for the 40 nm-pitch profile, and Equation (1a) is substituted by:

$$l' = 2\delta_1 + 2\delta_2 + (\lambda - 2\delta_1 - 2\delta_2 \cos \alpha) \tag{3}$$

Equation (2), thus, becomes:

$$\varepsilon_x \approx \frac{2\delta_2}{\lambda}(1 - \cos \alpha) \tag{4}$$

and, consequently, the total stretching energy is given by:

$$\Phi_m = \frac{1}{2}Et\lambda b\varepsilon_x^2 \approx \frac{2Etb}{\lambda}\delta_2^2(1 - \cos \alpha)^2 \tag{5}$$

being E the in-plane Young's modulus of the graphene sheet, t its thickness and b its width.

The total adhesion energy is given by:

$$\mathrm{U}_{adh} = -4\gamma b(\delta_1 + \delta_2) \tag{6}$$

where γ is the adhesion energy per unit area.

Finally, from the condition:

$$\frac{\partial(\Phi_m + \mathrm{U}_{adh})}{\partial \delta_2} = 0 \tag{7}$$

The adhesion energy per unit area, i.e.:

$$\gamma \approx \frac{Et}{\lambda}(1 - \cos \alpha)^2 \delta_2 \tag{8}$$

The Table below reports the results of the estimation of the strain and of the adhesion energy for the three considered profiles, where we have used $E = 1$ TPa and $t = 0.34$ nm.
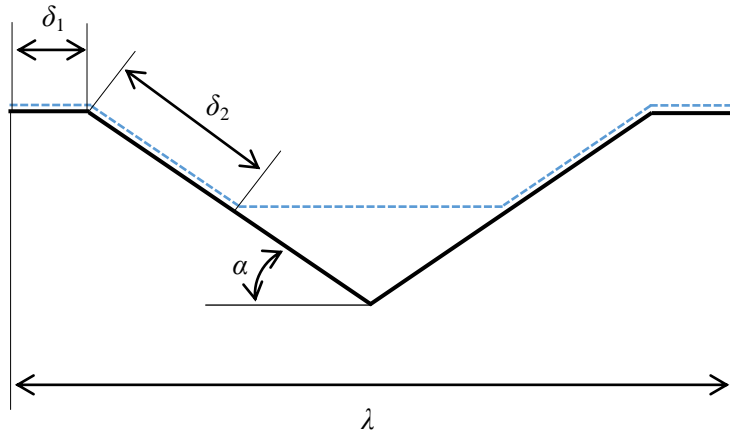
Figure S1: Schematic illustration of sagging graphene in the trough region between two grooves. λ (nm) is the spacing between the grooves of flat graphene. The parameters δ_1, δ_2 and α are associated to the adhesion of graphene between the grooves.

Table S 1: Quantitative evaluation/ Estimation of conformation induced average strain and adhesion energy for GrP40, P125 and P250.

	40 nm pitch	125 nm pitch	250 nm pitch
wavelength	$\lambda \approx 40$ nm	$\lambda \approx 125$ nm	$\lambda \approx 270$ nm
fit parameters	$A \approx 0.77$ nm	-	-
geometrical parameters	$\delta_1 \approx 0$ nm $\delta_2 \approx 11.7$ nm $\alpha \approx 7.6°$	$\delta_1 \approx 25$ nm $\delta_2 \approx 30.2$ nm $\alpha \approx 6.1°$	$\delta_1 \approx 105$ nm $\delta_2 \approx 30.2$ nm $\alpha \approx 6.7°$
average strain	$\varepsilon_x \approx 0.33$ %	$\varepsilon_x \approx 0.27$ %	$\varepsilon_x \approx 0.15$ %
reference compressive strain (graphene on flat)	$\varepsilon_c \approx -0.09$ %	$\varepsilon_c \approx -0.09$ %	$\varepsilon_c \approx -0.09$ %
adhesion energy	$\gamma \approx 0.0077$ J m$^{-2} \approx$ ≈ 0.48 meV Å^{-2}	$\gamma \approx 0.0026$ J m$^{-2} \approx$ ≈ 0.16 meV Å^{-2}	$\gamma \approx 0.0018$ J m$^{-2} \approx$ ≈ 0.11 meV Å^{-2}

We observe, as expected, that the average strain decreases for an increasing pitch of the texture substrate. This is due to the fact that the graphene sheet is not constrained between closer peaks, as instead happens for the 40 nm pitch. For the 250 nm pitch, in fact, the graphene sheet adheres completely to the substrate. We observed that the estimated adhesion energy per unit area is always in the same order of magnitude but it shows a decreasing trend with increasing wavelength of the profile. Note that the ion implantation process has heavily modified the SiO_2 surface, thus the order-of-magnitude of estimated adhesion energy is reasonable with values available in literature. For instance, Sabio et al.[3] estimated an interaction energy of 0.4 meV Å^{-2} for graphene on SiO_2 on the basis of electrostatic interactions. Aitken and Huang showed that the effective adhesion energy of monolayer graphene on an oxide substrate also depend on the surface corrugation[4].

S3. Calculation of strain and doping from Raman modes in Graphene

The strain (ε) and the charge carrier concentration (n) of graphene are related to the Raman shift (ω_1, ω_2) as presented in equation (1)[5,6].

$$\begin{pmatrix} \omega_1 \\ \omega_2 \end{pmatrix} = T \begin{pmatrix} \varepsilon \\ n \end{pmatrix} \qquad (1)$$

Where

$$T = \begin{pmatrix} -2\gamma_1\omega_1^0 & k_1 \\ -2\gamma_2\omega_2^0 & k_2 \end{pmatrix} \qquad (2)$$

γ is the Grüneisen parameter, k is the doping shift rate and ω^o is the no-strain and no-doping peak position. The subscript denotes the corresponding Raman modes. In graphene, ω_1 subscript *(1)* and $\omega_1(2)$ are G and 2D modes, respectively, where γ_G =1.95, γ_{2D} = 3.15, $k_G = -1.407 \times 10^{-12} cm^{-1}$ and $k_{2D} = -0.285 \times 10^{-12} cm^{-1}$ [5,7]. In fact, the vector space of Raman peak positions ω_1-ω_2 is a linear transformation from the ε-n space, while the origin of both spaces defines the absence of strain and doping. Therefore, ω represents the deviation of the recorded frequency from ω^0 due to strain or doping. It is to be noted that n represents the relative shift in the charge carrier and mostly originates from the charge exchange with the substrate. Also, the airborne impurities adsorb over the surface and at edge region may influence n.
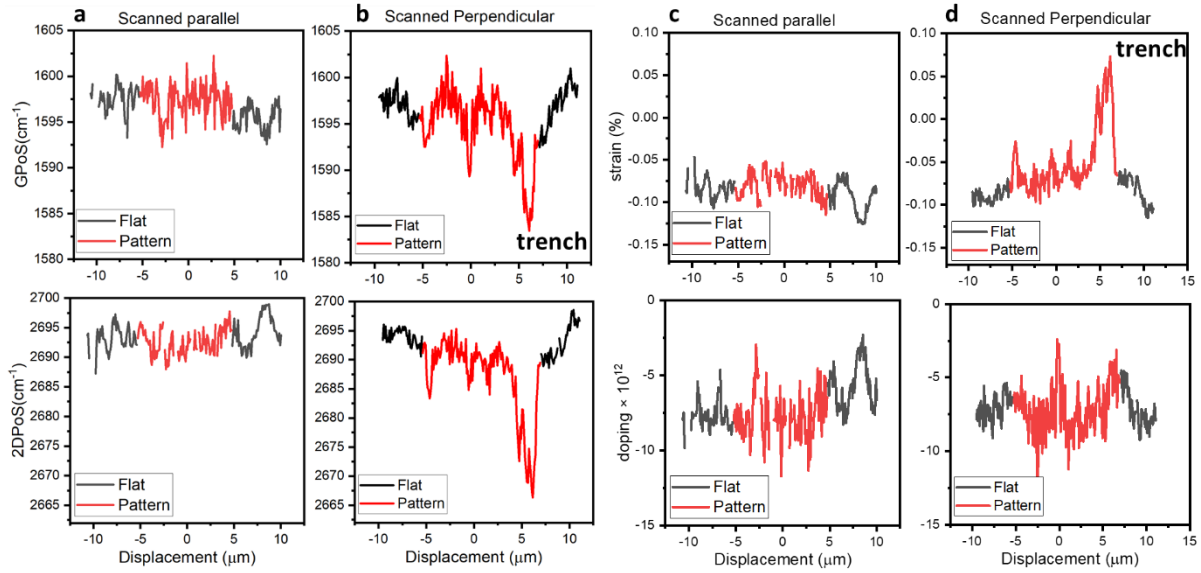

Figure S2: Raman line map scanning parallel and perpendicular to the groove axis of fixed P200. Distribution of Raman modes (Pos G, Pos 2D) over (a) parallel to the groove axis (red line) and (b) perpendicular to the groove axis. The flat Si surface used as reference to monitor the shift in peak position from flat to textured region. (c) The strain and doping line map illustrate a small change in strain and doping distribution along scanning parallel to groove axis. (d) There is a reduction of compressive strain (at flat surface) over the textured region. There is a slight change in doping at the texture region. The trech region at the end of textured surface shows a significant change strain and doping in the graphene.

S4. Molecular Dynamics and density functional theory: The atomic scale feature of graphene conformation over textured silicon surfaces is investigated through molecular dynamics (MD) and density functional theory (DFT) calculations of the graphene/Si composite system in different configurations. Initially, we have performed DFT calculations of bulk silicon and monolayer graphene in order to evaluate appropriate MD potential through comparison of structural properties. DFT calculations are performed using the Quantum ESPRESSO software[8,9]. Vanderbilt ultrasoft pseudopotentials[10] were employed, with a wavefunction cutoff of E_{cut} = 80 Ry, a Fermi-Dirac smearing of width 0.01 Ry, and a dense Monkhorst-Pack k-point grid sampling of *17x17x17* for bulk Silicon in a cubic supercell and *17x17x1* and for an isolated graphene monolayer in a hexagonal supercell. In the latter case, care is taken to introduce sufficient space between adjacent monolayers by using a large, fixed z-direction spacing of 25 Å, so there is no interaction between adjacent periodic images. Our calculations find lattice constants a_{Si} = 0.388 nm and c_{Si} = 0.541 nm in bulk silicon (see **Figure S2**) and a_{Gr} = 0.245 nm for the isolated graphene monolayer, with associated bond lengths b_{Si-Si} = 0.237 nm and b_{C-C} = 0.142 nm.

MD calculations were performed using the LAMMPS MD suite[11]. We have opted for the Stillinger-Weber potential for bulk Silicon[12], parameterized according to the GGA-DFT calculations of Lee and Hwang[13], which provides a better approximation of elastic properties such as the restoring forces on displaced atoms[14,15]. Graphene carbon interactions have been simulated using the LCBOP potential[14]. These potentials are chosen on the basis that they can reproduce DFT and experimental[16,17] lattice constants and bond lengths to a high degree of accuracy, which is crucial in resolving accurate structural properties. For example, our simulations find b_{Si-Si} = 0.238 nm and b_{C-C} = 0.1419 nm for silicon and graphene respectively, which is essentially in perfect agreement to the quantum calculations. The carbon-silicon interaction has been implemented using a Lennard-Jones 6-12 potential with ε_{Si-C} = 8.909 meV and σ_{Si-C} = 0.3326 nm to model physisorption of the graphene monolayer on a silicon substrate[16,18].
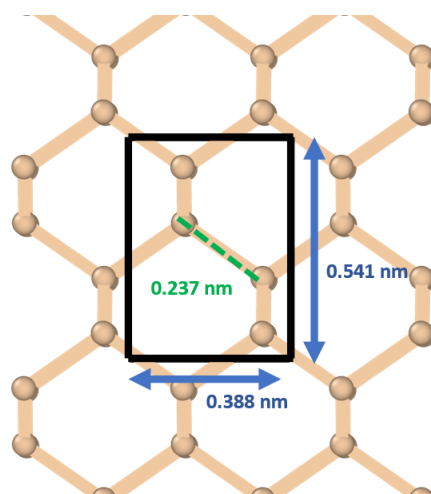

Figure S3. DFT-calculated structure of bulk Silicon. Lattice constants and the Si-Si bond length are indicated.

To investigate the effect of different textured silicon surfaces have on adsorption and strain of a graphene monolayer, different Gr/Si-lattice-matched simulation cells are constructed with and without nanometre-scale trenches, introduced into the silicon substrate through the removal of atoms. This necessarily requires the use of large cells in order to obtain satisfactory trench depth and to perform lattice-matching between the graphene and silicon unit cells, along the *x* (long) and *y* (small) axes (as shown in **Figure S4a**). Table 2 lists the graphene and Si cell dimensions and unrelaxed cell lengths for all of the structures we have simulated, as well as the corresponding initial lattice mismatch. For the P40 cell only, we have also considered a number of different lattice-matching conditions along the y-axis in order to check the consistency of our results and find very similar variation in bond and strain properties upon full relaxation. In all cases, the graphene layer is deposited along the (001) surface of silicon, and the graphene sheet is long in the [1010] (armchair) direction. For the largest cells, which are used to model the P250 textured surfaces, the cells employed contain approximately 370,000 atoms. The simulation cell used to model the P40 structure is shown in **Figure S4**.

Table 2: Details of different simulation cells used in this work. The cell lengths of the graphene and silicon structures, used for the P40, P125 and P250 textures are shown in their respective columns, with the corresponding number of unit cells shown in square brackets. Equilibrium graphene and silicon lengths in the x- and y-directions, associated initial mismatch, and the depth of the silicon slab are also shown.

Cell	Graphene X	Graphene Y	Silicon X	Silicon Y	x_{strain}	y_{strain} (%)	Depth

					(%)		(nm)
P40	39.614 nm [93]	3.197 nm [13]	39.670 nm [102]	3.111 nm [8]	0.1412	-1.3773	5
P40	39.614 nm [93]	3.935 nm [16]	39.670 nm [102]	3.889 nm [10]	0.1412	-0.5869	5
P40	39.614 nm [93]	4.667 nm [19]	39.670 nm [102]	4.672 nm [12]	0.1412	-0.0600	5
P125	125.234 nm [294]	3.197 nm [13]	125.234 nm [322]	3.111 nm [8]	0.0003	-1.3773	10
P250	250.468 nm [588]	3.197 nm [13]	250.468 nm [644]	3.111 nm [8]	0.0003	-1.3773	10

In order to approximate the experimental textured surfaces, we have introduced a nanometre-scale trench into the silicon substrate and extrapolated the change in lattice parameters upon geometric optimisation of all atoms for a flat (**Figure S4b**) and textured (**Figure S4c**) silicon slab. A trench of width 20nm and depth 3nm is used for the P40 configuration, while trenches of width 40nm and depth 5nm are used for the P125 and P250 configurations, in order to mimic the experimental configuration.

For all of the flat geometries, we find that the silicon slab causes a compression of the graphene monolayer. Notably, for the flat P125 and P250 geometries, which contain very little strain from lattice-matching of the graphene monolayer to the Si substrate, we find a minimal additional compression of around 0.12% (blue color in z-scale bar) of the average graphene bond length with respect to a perfect free-standing monolayer, which is in very good agreement with the experimental Raman data. Upon relaxation of the suspended geometries, we find configurations which give a close approximation to the partially-conformal morphologies of a graphene monolayer over a grooved substrate[19].
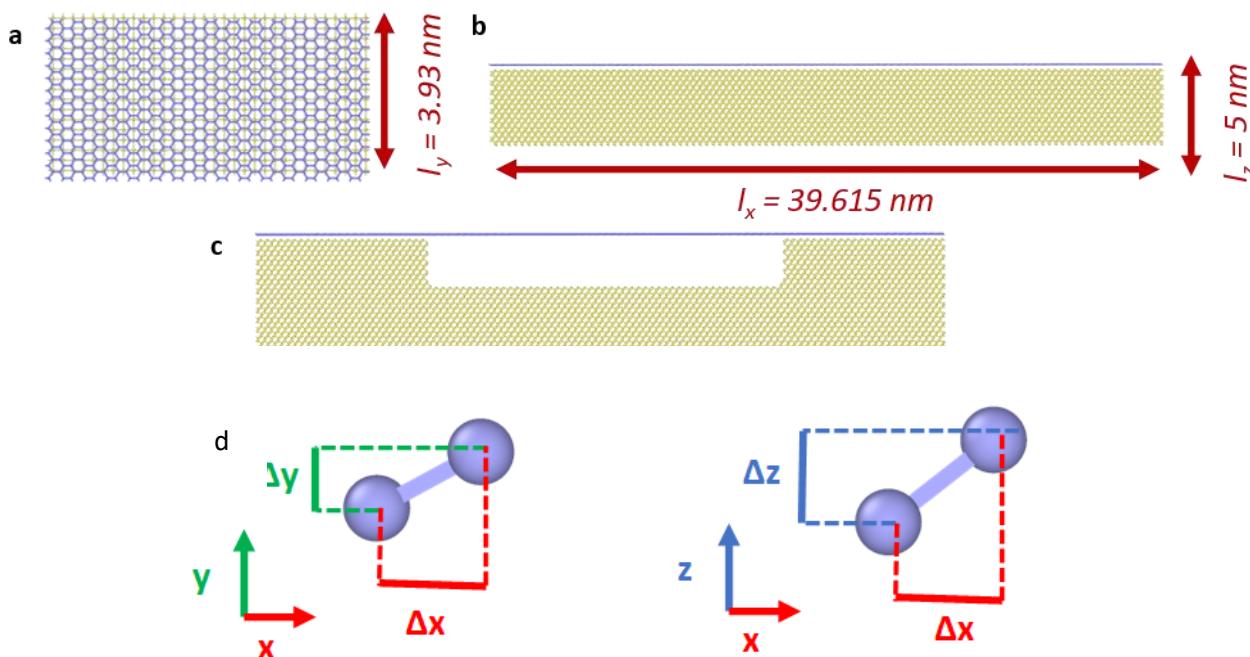

Figure S4. a) Top view of the perfect (i.e. without any surface texturing) P40 simulation cell and b) side view. The cell dimensions employed in our simulations are listed, for details of the number of unit cells used in this construction, see

Table 2. c) Initial configuration of the P40 graphene/silicon trench structure used to simulate the experimental textured surfaces. The corresponding relaxed geometries are shown in the main text, **Figure. 4 c-f**. (d) Schematic illustration of carbon atoms with a random orientation for the measurement of bond lengths.

We note that there are different distributions of strain across the flat (crest) and buckled (trough) regions, with bond variations. A full analysis of the local variation in the bond and strain distribution for the grooved P40 geometry has been carried out and is shown in the main text **Figure 4 c-f**. The bond length has been calculated between adjacent carbon atoms using the formula $b_0 = \sqrt{\Delta x^2 + \Delta y^2 + \Delta z^2}$, where Δx, Δy and Δz are the cartesian components of the distance between pairs of carbon atoms. Schematically, they are calculated as follows for an isolated pair of carbon atoms with a random orientation at figure S4 (d): The changes in Δz is due to alteration in the height of the graphene sheet above the Si substrate, while Δx and Δy reflect differences due to contact area and curvature. In Fig. 4 (main text), the latter two properties were extracted from MD data using a script, and total bond lengths were calculated using the OVITO program[20]

The local changes in the parallel and perpendicular strains have been extracted from the local bonds through comparison of the values of the Δx and Δy bond components to the values of a bond with the same angular orientation with a bond length equal to that of graphene adsorbed on a flat Si surface (i.e. compressed by 0.11% w.r.t free-standing graphene). The net changes in bond length (**Figure 2d** in main text) were calculated by averaging the C-C b_0 for carbon atoms in the crest, trough and across the entire cell.

S5. AFM and FFM calibration: Calibration of normal and torsional spring constants was done regularly at the beginning and during friction measurements according to Sader method[21,22]. Tip apexes were systematically estimated performing blind tip reconstruction by NT-MDT software (i.e. deconvolution of the topography image obtained on a special calibration grating composed of random distributed nanometric tips, PA01/NM by NT-MDT). Few tips were also imaged by scanning electron microscopy (SEM). Tips height was controlled by SEM images and found equal to the nominal value with a deviation of the order of 5%. The nominal value of 16 nm was used for all our tips.

Blind tip reconstruction and SEM images are presented on **Figure S5**. Tips parameters are presented on Table S2.
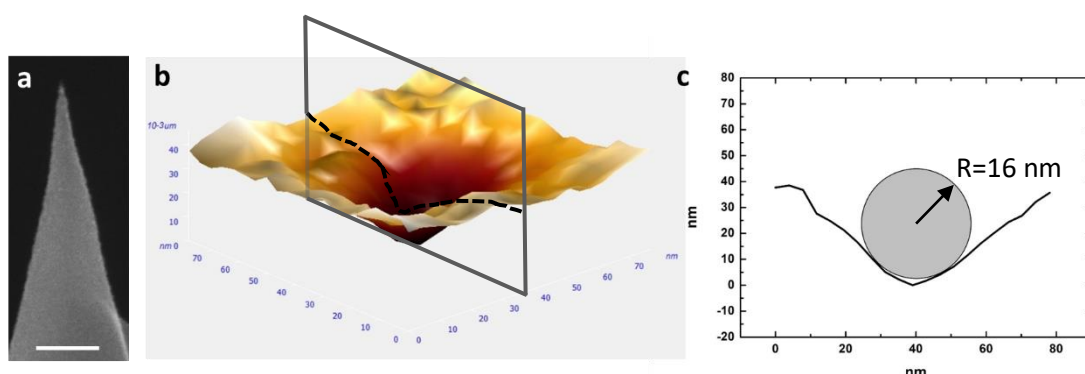

Figure S5. a) Representative SEM image of a new tip apex. scale bar 100nm; b) 3D blind tip reconstruction during FFM measurements; c) Tip profile extracted from 3D reconstruction and evaluation of the curvature radius.

Table S 2: Measured parameters of few relevant tips used during the experiment

Tip	K_{norm} (N/m)	K_{tors} (N m) 10^{-8}	Radius (nm)	Height (µm)
B6_b	0,26	1,06	19 ± 1	16 ± 1
B7_b	0,25	1,09	27 ± 2	16 ± 1
B9_b	0,23	1,05	21 ± 1	16 ± 1
B10_a	0,76	1,53	23 ± 1	16 ± 1
B11_b	0,27	1,08	16 ± 1	16 ± 1
B13_b	0,25	1,10	19 ± 1	16 ± 1

Beams Length: a = 250 µm; b = 350 µm

Lateral force refers to a single lateral force signal, forward or backward as acquired from the microscope, properly calibrated[23]. Friction force resulted from the difference between forward and backward lateral force divided by two (standard TMR analysis). Images or maps were typically acquired at ~1 Hz scan rate, on a 1x1µm^2 area. To establish the normal load applied, force-distance curves were previously acquired to calculate the photodetector sensitivity along the vertical direction. The same sensitivity was used for calibrating the lateral force signal.

To obtain friction vs load curves, the orthogonal scans were acquired in "one line" mode (512 pts per lines) by decreasing the set point (i.e. decreasing the applied normal load) every forty lines from~30nN to the pull-off value whereas for the parallel scan, an entire image (512x 512 pts) for each normal load was acquired. In the orthogonal scans, the friction forces were averaged on approximately thirty lines corresponding to a constant applied normal load to produce one data point; in the case of parallel scans, friction force values were averaged on a selected area of interest containing a number of points comparable to that used for orthogonal friction data points.

All the areas analyzed have been previously mechanically cleaned with a cantilever different from that used for friction measurement, using a normal load (~50nN) greater than the highest load reported in the plot.

AFM image processing, including the three-dimensional display of data, was carried out using both the software provided by NT-MDT and the free modular software Gwyddion (version 2.55).

The typical friction responses of graphene deposited on flat region investigated in two different orientations are reported in **Figure S6**. 3D topography reconstruction (**Figure S6a**) highlights the presence of sub-nanometeric corrugations over the graphene surface; lateral force map (S5b) as well as its profile (**Figure** S6 c) show an almost constant trend without the occurrence of any periodic modulation. A very similar behavior has been observed on the same region rotated by 90 degrees (**Figure S6 d,e,f**), depicting comparable frictional force.
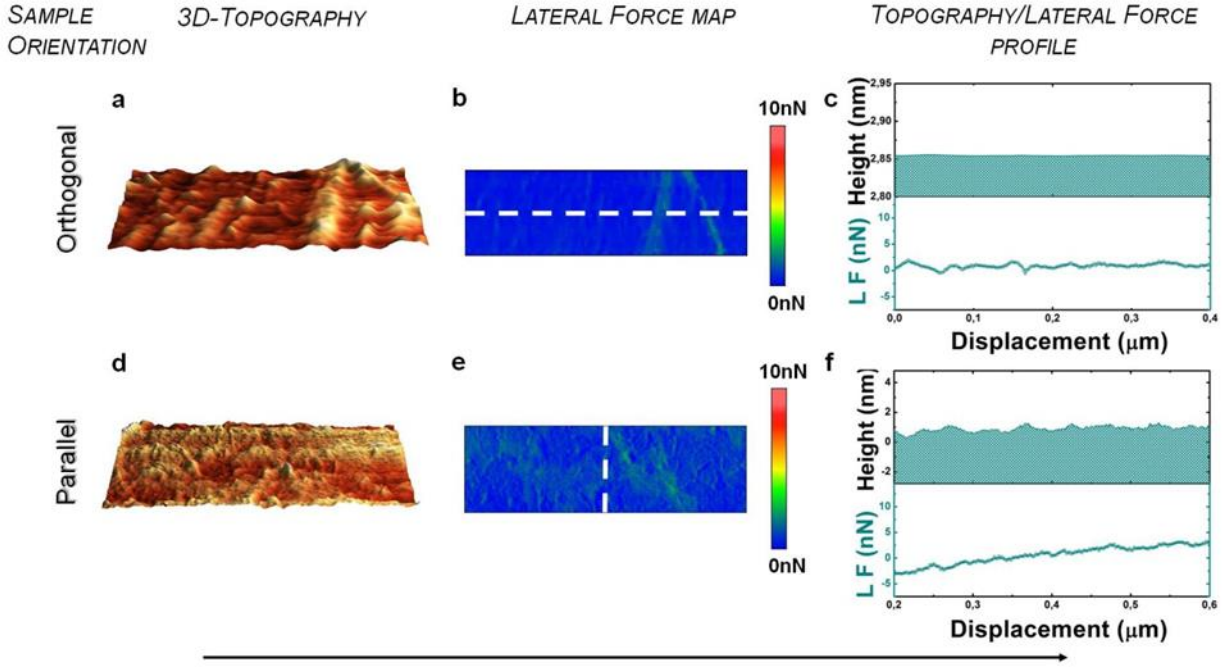
Figure S6. Effect of scan direction on lateral force for Gr flat region. (a) 3D topography image (1.0 x 0.5 micron) and (b) lateral force map (1.0 x 0.3 micron) measured simultaneously on flat region graphene-covered. Applied load ≈25nN. (c) Top, height profile and, bottom, corresponding lateral force (open dots correspond to raw data, dark cyan line is the result of 7 pts smoothing) extracted from white dashed line in (b); length 400nm. (d) 3D topography image (1.0 x 0.5 micron) and (e) lateral force map (1.0 x 0.3 micron) measured simultaneously on flat region graphene-covered rotated by 90° degrees. Applied load ≈25nN. (f) Top, height profile and, bottom, corresponding lateral force profile extracted from white dashed line in (e); length 400nm.

S6. Friction vs load curves fitting procedure: The procedure utilized to fit friction versus load curves was tested on different flat regions next to the textured areas. The measured friction force F_f is displayed according to the method developed and described by Carpick *et al.*[24] where the square root of F_f normalized to F_o (friction force measured at zero applied load) is plotted as a function of external applied load L_{ext}

$$\sqrt{\frac{F_f}{F_0}} = \left(\frac{a + \sqrt{1 - \frac{L_{ext}}{L_0}}}{1 + a} \right)^{2/3}$$

The square root is because relation refers originally to contact radius variation with load (sphere on a flat surface) but using single asperity approximation ($F_f = \tau \cdot \pi r^2$) the equation can be implied for friction forces. An example is presented on **Figure S7**. Data are fitted leaving a and L_o (the pull-off force in a force-distance cycle) as a free parameters. The significance of a is to evaluate the contact behavior with respect to the JKR model (Johnson-Kendall-Roberts) corresponding to a close to one and to DMT model (Derjaguin-Mueller-Toporov) corresponding a close to zero. Finally, L_0 can be compared to experimental measurements and results from DMT data fitting in order to test consistency of the procedure. Test performed on 5 different regions always reveals a < 0.05 confirming the use of DMT approximation.
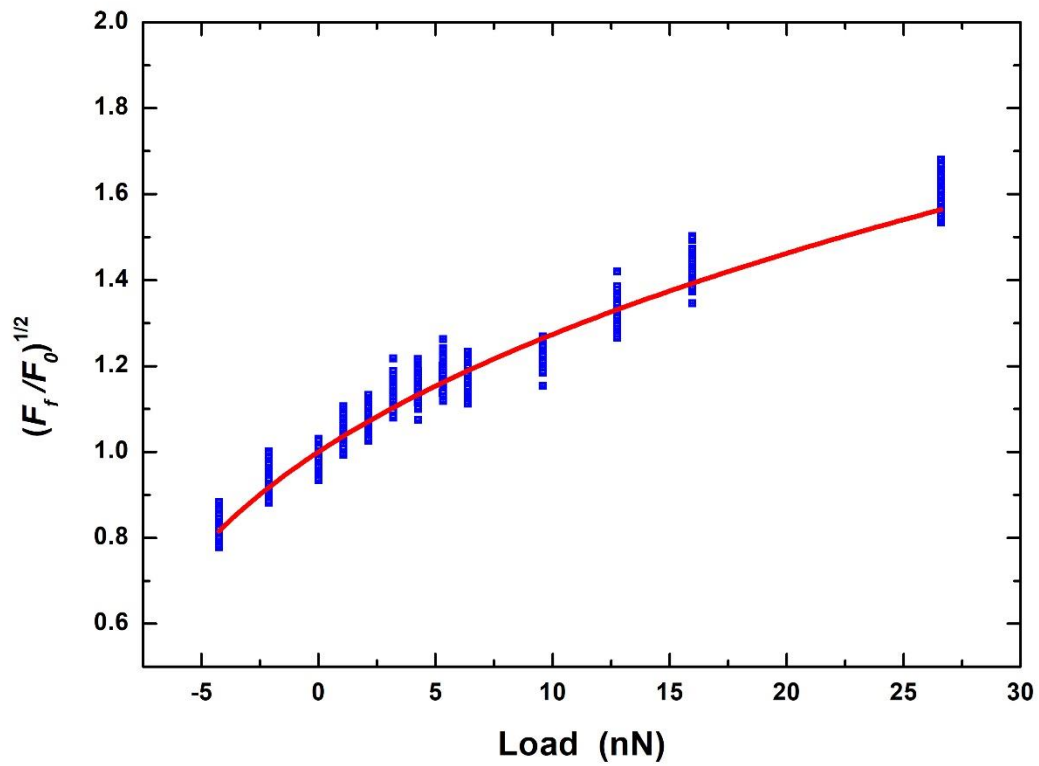
Figure S7. Blue dots represent the experimental data; Red curves is the fit according to method developed and described by Carpick et al.[24] where the square root of F_f normalized to F_o (friction force measured at zero applied load) is plotted as a function of external applied load L_{ext}. In this case we have $F_o = 4.25 \times 10^{-10}$ N and we obtain as fitting results $a = 0.001$ and $L_o = (-9.2 +- 0.7) \times 10^{-9}$ N (L_o is the pull-off force in a force-distance cycle).
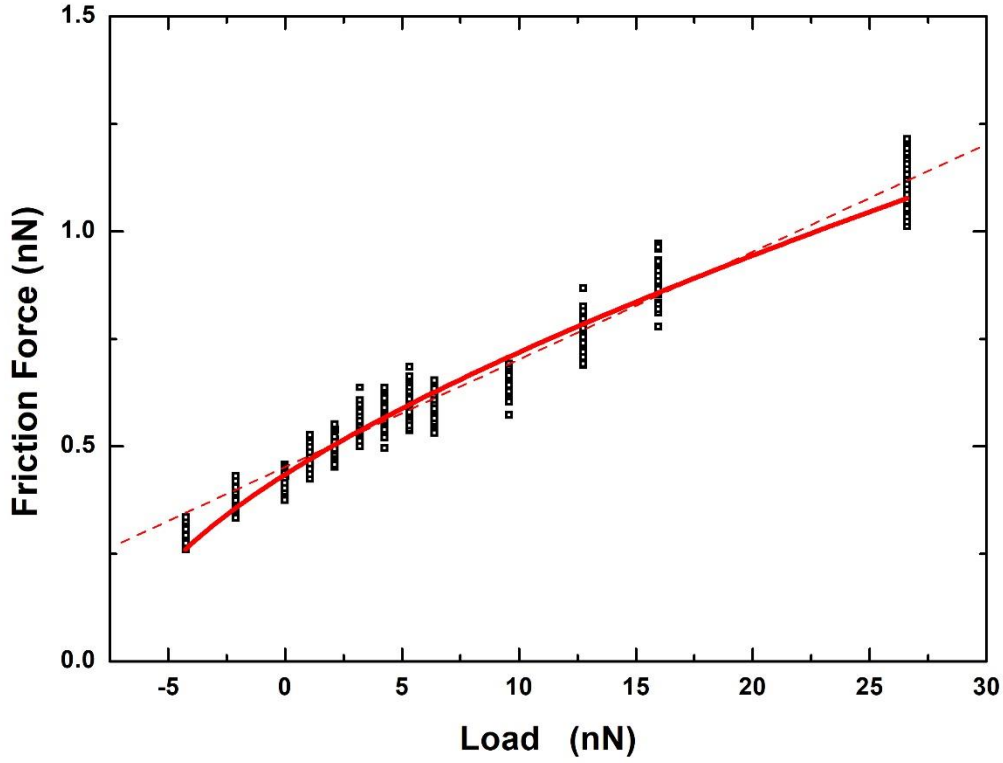
Figure S8. Black dots represent the raw data*;* red curve is the fitting curve according to DMT model + offset, red dashed line is the linear fitting.

In **Figure S8** raw data corresponding to curve at **Figure S7** and the corresponding DMT fitting curve are presented.

$$F_f = y_0 + A \cdot (L_{ext} + L_0)^{2/3}$$

where L_{ext} represent the external load, L_0 is the adhesion force and we add the offset y_0 to accounts for small but unavoidable non zero values of the photodetector lateral signal at zero applied load (i.e. far from the surface).

During fitting procedure the power law exponent is fixed at 2/3 and eventually L_0 was forced to the experimental pull off force value obtained by force – distance curve so that the outcome of this procedure is only the A parameter ($A = S \cdot \pi \cdot \left(\frac{3}{4} \cdot \frac{R}{K}\right)^{2/3}$) that contains information about shear strength S at the interface.

To evaluate quantitatively the shear strength S, the reduced Young's modulus of the interface (K) and the tip radius R have to be estimated. We used SEM images of tips apex and we performed blind tip reconstruction in connection with all friction vs load curves to evaluate R (see table 1). On the contrary the reduced Young's modulus K is estimated from tabulated values of mechanical parameters of the materials involved. The Young's modulus (E = 70 GPa) and Poisson's ratio (ν = 0.2) of the SiO_2 has been used for the tip apex and bare substrate[25]. Instead we used, in analogy with literature results[25,26] the bulk elastic constants of graphite (E = 30 GPa; ν = 0.24), for the single layer graphene deposited on SiO_2. Following these

approximations, we extract a shear strength of 25 MPa from the curve **Figure** S7. Similarly, we obtain the results summarised on Table 1 in the main text and the complimentary analysis on GrP(40) sample, location 2 presented on **Figure S9**.
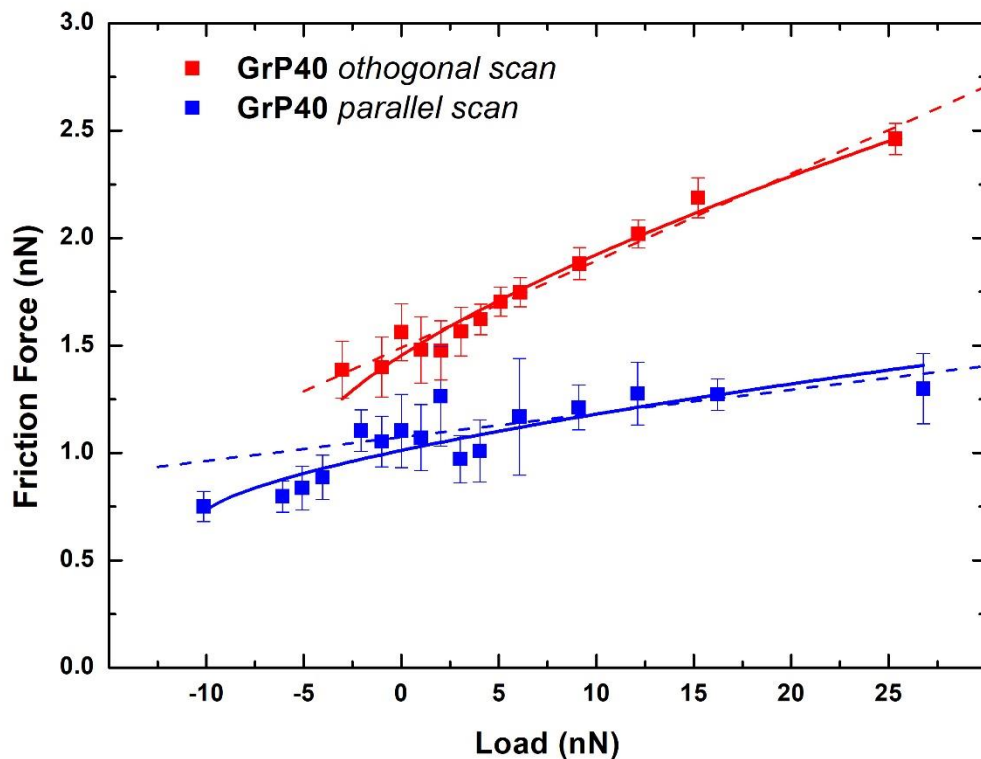

Figure S9. Load depended friction force on GrP40 sample with the grooves axis oriented parallel (blue) and perpendicular (red) to the fast scan direction. Analyzed area corresponds to a completely different region with respect to the one analyzed in **Figure 4** in the main text. Square dots represent the raw data while continuous lines are the fitting curve according to DMT model. The corresponding shear strength are 43 MPa and 17 MPa for sliding direction perpendicular and parallel to the texture respectively

References

(1)   Dell'Anna, R.; Iacob, E.; Tripathi, M.; Dalton, A.; Böttger, R.; Pepponi, G. *J. Microsc.* **2020**, No. 1, jmi.12908.

(2)   Dell'Anna, R.; Masciullo, C.; Iacob, E.; Barozzi, M.; Giubertoni, D.; Böttger, R.; Cecchini, M.; Pepponi, G. *RSC Adv.* **2017**, *7* (15), 9024–9030.

(3)   Sabio, J.; Seoánez, C.; Fratini, S.; Guinea, F.; Neto, A. H. C.; Sols, F. *Phys. Rev. B - Condens. Matter Mater. Phys.* **2008**, *77* (19), 1–8.

(4)   Aitken, Z. H.; Huang, R. *J. Appl. Phys.* **2010**, *107* (12), 123531.

(5)   Lee, J. E.; Ahn, G.; Shim, J.; Lee, Y. S.; Ryu, S. *Nat. Commun.* **2012**, *3*, 1024.

(6)   Michail, A.; Delikoukos, N.; Parthenios, J.; Galiotis, C.; Papagelis, K. *Appl. Phys. Lett.* **2016**, *108* (17), 173102.

(7)   Jiang, T.; Wang, Z.; Ruan, X.; Zhu, Y. *2D Mater.* **2018**, *6* (1), 015026.

(8)   Giannozzi, P.; Baroni, S.; Bonini, N.; Calandra, M.; Car, R.; Cavazzoni, C.; Ceresoli, D.; Chiarotti, G. L.; Cococcioni, M.; Dabo, I.; Dal Corso, A.; De Gironcoli, S.; Fabris, S.; Fratesi, G.; Gebauer, R.; Gerstmann, U.; Gougoussis, C.; Kokalj, A.; Lazzeri, M.; Martin-Samos, L.; Marzari, N.; Mauri, F.; Mazzarello, R.; Paolini, S.; Pasquarello, A.; Paulatto, L.; Sbraccia, C.; Scandolo, S.; Sclauzero, G.; Seitsonen, A. P.; Smogunov, A.; Umari, P.; Wentzcovitch, R. M. *J. Phys. Condens. Matter* **2009**, *21* (39).

(9)   Giannozzi, P.; Andreussi, O.; Brumme, T.; Bunau, O.; Buongiorno Nardelli, M.; Calandra, M.; Car, R.; Cavazzoni, C.; Ceresoli, D.; Cococcioni, M.; Colonna, N.; Carnimeo, I.; Dal Corso, A.; de Gironcoli, S.; Delugas, P.; DiStasio, R. A.; Ferretti, A.; Floris, A.; Fratesi, G.; Fugallo, G.; Gebauer, R.; Gerstmann, U.; Giustino, F.; Gorni, T.; Jia, J.; Kawamura, M.; Ko, H.-Y.; Kokalj, A.; Küçükbenli, E.; Lazzeri, M.; Marsili, M.; Marzari, N.; Mauri, F.; Nguyen, N. L.; Nguyen, H.-V.; Otero-de-la-Roza, A.; Paulatto, L.; Poncé, S.; Rocca, D.; Sabatini, R.; Santra, B.; Schlipf, M.; Seitsonen, A. P.; Smogunov, A.; Timrov, I.; Thonhauser, T.; Umari, P.; Vast, N.; Wu, X.; Baroni, S. *J. Phys. Condens. Matter* **2017**, *29* (46), 465901.

(10)   Giannozzi, P.; Baseggio, O.; Bonfà, P.; Brunato, D.; Car, R.; Carnimeo, I.; Cavazzoni, C.; De Gironcoli, S.; Delugas, P.; Ferrari Ruffino, F.; Ferretti, A.; Marzari, N.; Timrov, I.; Urru, A.; Baroni, S. *J. Chem. Phys.* **2020**, *152* (15).

(11)   Garrity, K. F.; Bennett, J. W.; Rabe, K. M.; Vanderbilt, D. *Comput. Mater. Sci.* **2014**, *81*, 446–452.

(12)   Plimpton, S. *J. Comput. Phys.* **1995**, *117* (1), 1–19.

(13)   Stillinger, F. H.; Weber, T. a. *Phys. Rev. B* **1985**, *31* (8), 5262–5271.

(14)   Lee, Y.; Hwang, G. S. *Phys. Rev. B* **2012**, *85* (12), 125204.

(15)   Jing, Y.; Hu, M.; Guo, L. *J. Appl. Phys.* **2013**, *114* (15), 153518.

(16)   Los, J. H.; Fasolino, A. *Phys. Rev. B* **2003**, *68* (2), 024107.

(17)   Graziano, G.; Klimeš, J.; Fernandez-Alonso, F.; Michaelides, A. *J. Phys. Condens. Matter* **2012**, *24* (42), 424216.

(18)   Kaftory, M.; Kapon, M.; Botoshansky, M. In *Wiley, Chichester*; 1998; Vol. 121, pp 181–265.

(19)   Ong, Z.-Y.; Pop, E.; Shiomi, J. *Phys. Rev. B* **2011**, *84* (16), 165418.

(20)   Stukowski, A. *Model. Simul. Mater. Sci. Eng.* **2010**, *18* (1), 015012.

(21)   Sader, J. E.; Chon, J. W. M.; Mulvaney, P. *Rev. Sci. Instrum.* **1999**, *70* (10), 3967–3969.

(22)   Green, C. P.; Lioe, H.; Cleveland, J. P.; Proksch, R.; Mulvaney, P.; Sader, J. E. *Rev. Sci. Instrum.* **2004**, *75* (6), 1988–1996.

(23)   Gnecco, E.; Pawlak, R.; Kisiel, M.; Glatzel, T.; Meyer, E. In *Nanotribology and Nanomechanics*; Springer International Publishing: Cham, 2017; pp 519–548.

(24)   Carpick, R. W.; Ogletree, D. F.; Salmeron, M. *Area* **1999**, *400*, 395–400.

(25)   Buzio, R.; Gerbi, A.; Uttiya, S.; Bernini, C.; Del Rio Castillo, A. E.; Palazon, F.; Siri, A. S.; Pellegrini, V.; Pellegrino, L.; Bonaccorso, F. *Nanoscale* **2017**, *9* (22), 7612–7624.

(26)   Deng, Z.; Klimov, N. N.; Solares, S. D.; Li, T.; Xu, H.; Cannara, R. J. *Langmuir* **2013**, *29* (1), 235–243.